High Dynamic Range in Entomological Scheimpflug Lidars

Mikkel Brydegaard [iD], Benoit Kouakou [iD], Samuel Jansson [iD], Jens Rydell, and Jeremie Zoueu

Abstract—Minimizing insecticide use, preventing vector diseases and facilitating biodiversity assessments are suitable applications of recent advances in photonic insect surveillance and entomological lidar. The tools also comprise a new window into fundamental aspect of the fascinating life and ecology of insects and their predators *in situ*. At the same time, it is evident that lidars are subject to finite detection range given by the instrument noise and saturation levels, and therefore, intervals of the biomass spectra are sectioned at different ranges. The Scheimpflug lidar allows an interesting trade-off between high sample rate and low pulse energy for retrieving wing beat harmonics and slow sample rates with high pulse energy for detecting small species far away. In this paper, we review and revise calibration, sizing and associated deficiencies, and report count rates to 10^4 insects/minute up to 2 km range. We investigate if and how high dynamic range can be exploited in entomological lidar and also how fast and slow sample rates could complement each other and capture a wider span of the biomass spectrum. We demonstrate that smaller insect can be detected further away by long exposures and show consistency between the captured biomass size spectra. However, we find unexpected discrepancies between short and long exposures in the range distributions. We found that vertebrates as well as specular insects can saturate signals. Error sources and limitations are elaborated on.

Index Terms—Aerofauna, biophotonics, ecology, entomology, environmental monitoring, laser radar, lidar, remote sensing.

I. BACKGROUND AND MOTIVATION

THE changing climate and the ongoing anthropogenic conversion of the biosphere [1] leads to extinction of pollinating insects as well as invasion of new territories by pests

Mikkel Brydegaard is with the Department of Physics and Biology, Lund University, Lund, Sweden, and also with the Norsk Elektro Optikk, 0667 Oslo, Norway (e-mail: mikkel.brydegaard@fysik.lth.se).

Benoit Kouakou and Jeremie Zoueu are with the Felix Houphouet-Boigny Institute, at the Instrumentation,Imaging and Spectroscopy Laboratory, Yamoussoukro, Ivory Coast BP1093, Yamoussoukro (e-mail: benoitkouakou@gmail.com; jzoueu@yahoo.fr).

Samuel Jansson is with the FaunaPotonics, 2450 (Copenhagen, Danmark) and Dept. of Physics and Biology, Lund University SE-22363, Lund, Sweden (e-mail: saja@faunaphotonics.com).

Jens Rydell is with the Dept. Biology, Lund University, SE22363 Lund, Sweden (e-mail: jens.rydell@telia.com).

and disease vectors. Pesticide overuse and light pollution [2] pushes beneficiary insects and insectivores back towards the few remaining nature reserves, particularly in the tropics [3]. A rapidly changing world requires swift measures for conservation ecology which in turn set demands for rapid diagnostics tools *in situ*. However, when it comes to entomological surveys we find ourselves blinded from the grand overview; what species to catch? Which trap design and lure to use? How many? Where to position traps in the landscape and when to empty and with what frequency? The analysis of trap catches will take months of work by dedicated experts, even in a limited study.

This calls for engineering solutions and, hence, insect surveillance was pursued from the 1970s by radar [4], [5]. Important insights in insect migration insects have been revealed [6] as well as clues to target identity [7]. However, clutter constrains the applicability of radar near the ground.

Distributed sensors, or E-traps, have been proposed [8]–[11] including commercial initiatives [12], [13]. Much of the discussion regarding positioning of the trap, the lure and species biasing is, however, well known from the use of conventional traps.

Entomological laser radar [14], hereafter called lidar, emerged 15 years ago [15], [16]. In particular, the Scheimpflug lidar concept [17]–[19] greatly increased the efficiency of counting insects *in situ* [20]–[22]. Implementation of multiple wavelength [23]- or polarization [24]-bands makes it possible to interact with molecules and microstructure in distant insects and improve target classification [25]–[27]. Although the lidar penetration into the phylogenetic tree cannot be compared to microscopic and genetic analysis of trap catches or sweep netting, the classification can in principle be instantaneous and lidar can provide a representative picture of flight activity across all species. Lidar also makes it possible to study species over a large size span from midges to birds and bats [20], [28], [29].

The optical power of E-traps and entomological lidars does not differ noticeably, but the great advantage of lidars is that the laser light is recycled meter after meter, thus a relatively large probe volume can be trans-illuminated by sufficient intensity. Consequently, lidars yield insect counts several orders of magnitudes higher than E-traps. Whereas radar echoes decrease by r^4, since both the beam and the backscatter diverge, lidar signals are generally thought to decrease by r^2 since only the backscatter diverges. This is, however, not necessarily true for flat and specular targets [30], [31], including insect wings [32], and effects of this will be presented in this report.

TABLE I
VARIABLES, VALUES AND UNITS

Symbol	QUANTITY	Value	Unit
EXPERIMENTAL CONDITIONS:			
r	Range from lidar	35..2000	m
r_{term}	Range to calibration target	516	m
R_{term}	Reflectance of calib. target	1.8	%
f_s	Line rate	3000 & 300	Hz
τ	Exposure time	310 & 3313	µs
E_0	Laser energy/exposure	0.3 & 2.8	mJ
c	Speed of light	299792	kms^{-1}
n_{air}	Refractive index of air	1.003	-
μ_s	Atmospheric scatter	0.11	km^{-1}
SCHEIMPFLUG LIDAR SPECIFICATIONS:			
-	Baseline separation	814	mm
λ	Wavelength of the lidar	808 ±2	nm
P	Laser diode peak power	3 @ 3A	W
ℓ_{LD}	Laser emission chip size	9*x200	µm
$\varnothing_{exp}$	Expander aperture	102	mm
F_{exp}	Expander focal length	500	mm
η	Expander output coupling	28	%
$\varnothing_{rec}$	Receiver aperture	204	mm
F_{rec}	Receiver focal length	800	mm
-	Detection filter	808 ±3	nm
θ_{sens}	Sensor tilt	45	°
ℓ_{pix}	Pixel size	14x200	µm
p	Pixels	1..2048	#
H_{prob}	Height of probe volume	~100	mm
W_{prob}	Width of probe volume	10..500	mm
CALIBRATION AND ANALYSIS VARIABLES:			
r_0	Range of half overlap	79.4	m
S	Lidar sensitivity	5200	bits km mJ^{-1}
G	Instrument gain factors	0..1	-
I	Lidar intensity counts	0..2^{16}-1	16 bit
γ	Shape parameter form factor	1.8	-
σ	Backscatter cross section	10^{-2}..10^2	mm^2
δ	Apparent size	0.5..100	mm
Δt	Transit time	~10..1000	ms
α	Observed range dependence	1.2..2.2	-
R	Diffuse reflectance	~1..1000$^\square$	%
N	Number of insects	10^0..10^5	#
R^2	Adjusted goodness of fit	0-100	%

*diffraction limited size, $^\square$ for specular cases

In principle, lidars can be used vertically [29] or swept, to produce radial 2D scans [33]–[35] or spherical 3D scans [36]. In practice, there are few reports attempting to quantitatively evaluate and interpret range profiles of insects [35], [37]. A major challenge is the necessity of accurate knowledge of the beam shape at all distances and the handling of range dependent detection limits. The latter implies that specific sections of the aerofauna biomass spectrum is captured at different ranges.

In this paper we will first revise entomological lidar calibration. We will then explore benefits of high dynamic range by a comparative investigation of the detection limits for insect sizing and ranging for long and short exposures with high and low pulse energies respectively (See Table I). Interesting ecological aspects of how aerofauna activity changes during the course of the day in relation to vegetation and light pollution is also presented.

II. TEST RANGE AND INSTRUMENTATION

A. Test Range

The Ivorian Scheimpglug lidar [38] is positioned on the second floor in the Instrumentation, Imaging and Spectroscopy laboratory at Félix Houphouët-Boigny Institute, Yamoussoukro, Ivory Coast. It overlooks the Ivorian bush with agricultural patches with cassava and banana. Ground features also include mango trees, palms and termite mounds. At the campus, abandoned houses and a partly collapsed basement provide shelter for horseshoe bats and swallows. We report evening data from the late hot and dry season with stable and reproducible weather. The transect starts at 6°56'26.4"N 5°13'28.7" W and passes under the canopy of a huge silk-cotton *Ceiba* tree at 6°53'30.1"N 5°13'13.4"W located 516 m away and heading 84°. A black neoprene calibration target is mounted on the trunk of the tree. In order to avoid saturation in long exposure mode, the beam was directed off the target after calibration. The beam is horizontal and fluctuating between 6 m and 14 m above ground in the reported transect.

B. Scheimpflug Lidar

The instrument used is an entomological Scheimpflug lidar. The design resembles similar systems elsewhere [17], [19], [21], [22], [24], [37], [39]–[42]. Such systems comprise a baseline, mounted on a motorized tripod with a transmitter at one end and a receiver at the other. The specifications are given in Table I. The lidar data is acquired by a USB2 camera (Glaz LineScan1, Synertronic Design, South Africa) with a linear CMOS sensor (S11639-01, Hamamatsu, Japan). The device is controlled by a custom made interface, provided by the manufacturer. In this study, the sensor and lidar were operated at two distinct sampling rates of 300 Hz and 3000 Hz during two consecutive evenings. The sampling frequency and strobe signal in turn controlled the laser diode modulation, intensity is constant but respective laser energy per exposure is estimated to 2804 µJ and 225 µJ (see Table I).

III. DATA AND CALIBRATION

In this section we revise the data format and calibration procedures, including various refinements compared to our earlier reports [20], [39], [40].

A. Data format

Raw data is saved in files spanning 10 s each. These include 16 bit light intensity measurements, $I_{(r,t)}$, for 2048 pixel and either 3000 or 30000 exposures for 300 Hz and 3000 Hz sample rates respectively. The odd exposures, I_{odd}, include laser light, $I_{bright(r)}$, background light, $I_{bgr(r)}$, and dark current, $I_{dark(r)}$. The even exposures, I_{even}, include background light and dark current. Note that the dark current is denoted with range (pixel) dependency. This is because of structured dark current on CMOS and potential temperature gradients on the sensor.

We collected data during 4½ hours around sunset during two consecutive days with fast and slow sample rates, respectively. As we will see later, the day of slow sample rate was subject to artificial light-pollution. In Fig. 1, an overview of the dataset is presented. In these range-time maps each single column represents minimum-, median- and maximum- intensity values of
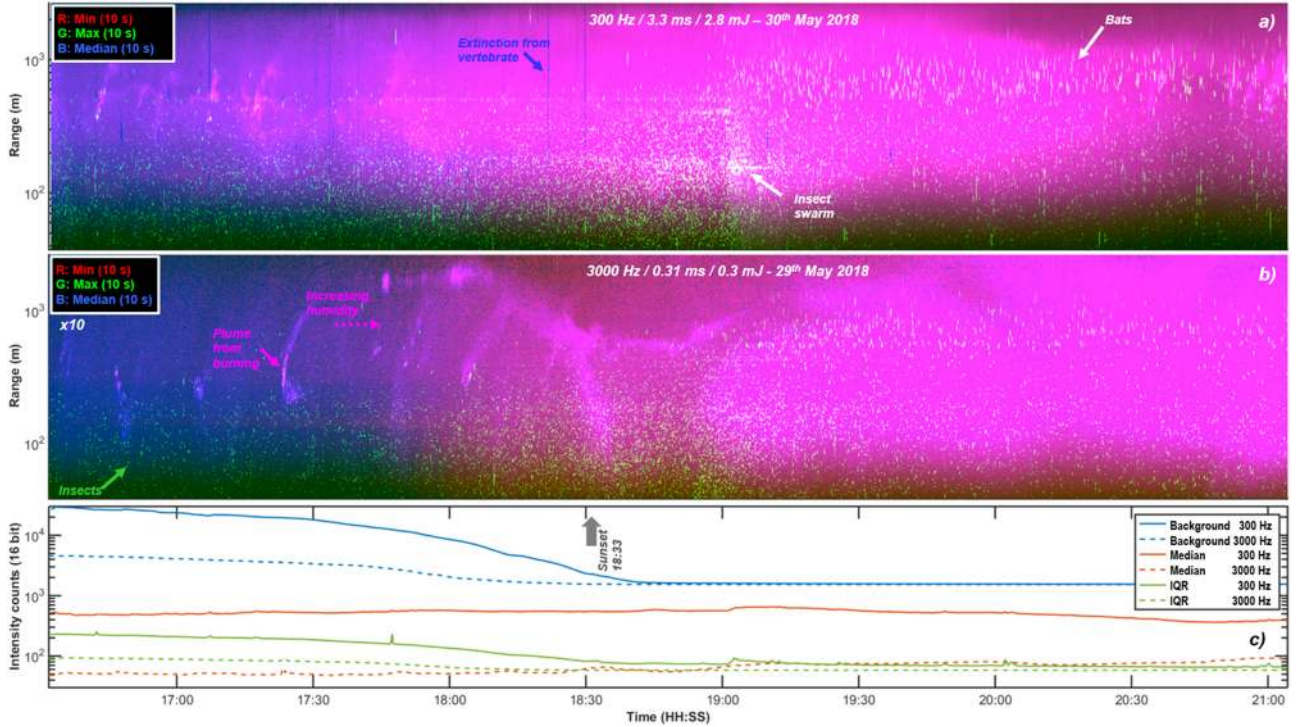
Fig. 1. Time-range overview maps of the two successive evenings reported. The maps are color-coded such that each column represent the temporal minimum-, median- and maximum- value for each pixel in each 10 s data file. Note that the range scale is logarithmic. During the evening the humidity and atmospheric scatter coefficient increases, this increases the static atmospheric echo reflected minimum and median by magenta color. Occasional plumes also affect the static air echo. Insects cause narrow spikes to the maximum signal and are seen as green dots. Large vertebrates can efficiently extinguish the entire beam, after which atmospheric echo diminishes. This is seen as blue lines in 1a. The brightness in 1b have been increased tenfold to compensate for the shorter exposure. The lower panel 1c, displays how the average properties of background sunlight (dark exposures), air signal (median) and noise (inter quartile range, IQR) changes throughout the evenings.

each 10 s file and is color-coded accordingly. This color-coding captures rare-events such as insects as bright dots.

B. Range Calibration and Resolution

Range calibrations are discussed in previous work [39], [40], [43], [44]. We calibrated the range, r, by the geometry of our lidar instrument and GPS coordinates of the lidar and a calibration target at 516 m distance. Due to the triangulating nature of Scheimpflug lidar, range resolution [43] is thought to deteriorate with $\tan(r)$ or approximately with r^2. However, the resolution also depends on the beam width [44], and by strategically choosing the beam expander size [19], it is possible to compensate for this deterioration by a converging beam and attain a linearly deteriorating range uncertainty typically in the order of 3% of r. The lidar beam can remain collimated (along the axis of the lidar baseline) up to the farfield limit, $r_{farfieldII} = \varnothing^2_{Exp} / 2.44 \lambda = 5$ km. Whereas range estimation at distances out to that of the calibration target is is fairly accurate, it can be expected that small inaccuracies can cause ranging error to drift when extrapolating to ranges beyond the calibration target. See further discussion [45].

C. Instrument Function and Atmospheric Return

In analogy to spectral response curves of spectrometers, lidars have a range response, referred to as the *lidar form factor*. This function is distinct for the distributed atmospheric propagation media and also for diffuse and specular hard targets. Because the depth of each successive probe volume of Scheimpflug lidars increases by r^2, the backscatter increases accordingly. This implies that the echo from the air or atmospheric return in Scheimpflug lidars are not subject to r^{-2} attenuation, as known from *Time-of-Flight* lidars. The atmospheric lidar formfactor is therefore equivalent to the fraction of laser light transilluminating each pixel footprint in the atmosphere. Due to beam expansion, the beam is typically wider than the *Field-of-View* at close distance. This is known as the region of incomplete overlap. The overlap function of Scheimpflug lidars can be expressed as:

$$G_{overlap(r)} = \frac{1}{1 + \left(\frac{r_0}{r}\right)^\gamma} \quad (1)$$

This sigmoidal response resembles previous analytical overlap functions [46] (1. is a hi-pass transfer function of order γ also known as the loglogistic or Fisk's cumulant). The r_0 denotes range of half overlap and γ is a steepness factor. For our setup, we found $r_0 = 79$ m and $\gamma = 1.8$. Previous work [19] gives a longer indication of complete overlap than $2r_0$. We note that it is comparable, but the previous estimate is based on geometrical optics and gives a longer and more restrictive value.

Scheimpflug lidars commonly employ synchronized *lock-in* detection for background rejection [18], [42], [47]. This implies that the laser is switched *on* and *off* between even and odd

exposures, and that the difference constitutes the lidar signals. As in ordinary lock-in detection, there can be a phase delay, φ, between the sampling (line array exposures) and the carrier wave after the round trip. Thus, φ is range dependent and with high sample rate the signal and dark timeslot will eventually swap for the distant pixels. This phenomena can be expressed and corrected for by a rotational matrix operation;

$$\begin{bmatrix} I_{bright(r)} \\ I_{bgr(r)} \end{bmatrix} = \begin{bmatrix} \cos & \sin \\ -\sin & \cos \end{bmatrix}^{\varphi(r)} \begin{bmatrix} I_{odd(r)} - I_{dark(r)} \\ I_{even(r)} - I_{dark(r)} \end{bmatrix} \quad (2)$$

$$\varphi(r) = \frac{\pi f_s r \, n_{air}}{c} + \varphi_{driver} \quad (3)$$

$$I_{sig(r,t)} = I_{bright(r,t)} - I_{bgr(r,t)} \quad (4)$$

Ideally there is no driver delays, but we detected $\varphi_{driver} = 0.9°$ @ $f_s = 300$ Hz and $4.1°$ @ $f_s = 3000$ Hz. This constitute a laser leak from odd to even exposures of 1.6% and 7% respectively. This depends on laser diode fall-times and can be fixed by improving the laser driver circuit, adjusting exposure times and read-out gap and by choosing the right polarity on the trigger flank. For now, this was corrected according to 2 to 4 and the specified φ_{driver}. Since the exposures and carrier wave are more squared than sinusoidal, the range dependent time-of-flight loss can be expressed as a triangle wave:

$$G_{ToF(r,f_s)} = 1 - \frac{4 f_s r \, n_{air}}{c} , \; 2 f_s r n_{air} < c \quad (5)$$

Our experiment employed a horizontal beam, and between occasional plumes from agricultural burnings, the signal is smooth in time and space, and the atmosphere can be assumed homogeneous. When this is the case, the expected lidar backscatter should attain the form:

$$G_{air(r,t)} = e^{-2\mu_{s(t)} r} \quad (6)$$

Since the 808 nm lidar band does not coincide with any absorption bands in the atmosphere, the attenuation coefficient entirely derives from scattering. Note that the scatter coefficient, μ_s, varies with temperature and humidity, and thus commonly changes during the evenings, see Fig. 1. At 808 nm, the minimal μ_s value is 0.0025 km^{-1} (molecular Rayleigh scattering), but typically the value varies between 0.1 km^{-1} in clear conditions to 10 km^{-1} in dense fog. The homogeneous air lidar signal can be found statistically by the time median [37] during clear conditions. When this is the case, it can be described accurately by the combined instrument function:

$$I_{air(r,t)} = E_0 \; S \mu_{s(t)} G_{air(r,t)} G_{ToF(r,f_s)} G_{overlap(r)} \quad (7)$$

Here, E_0 is the laser energy during the exposure and S is the lidar sensitivity. This analytic function yielded an explanation grade of 99.98% adjusted R^2 when fitted to the median homogeneous air signal, see example in Fig. 2. We encountered $S \approx 5.2$ kBits km mJ^{-1}. With our pulse energies, E_0, of 2.8mJ @ 300Hz and 0.3 mJ @ 3000 Hz and $\mu_s \approx 0.1$km^{-1}, we acquired respectively $I_{sig} \approx 1.1$ kBit and $I_{sig} \approx 0.1$ kBit, at complete overlap, for comparison the single shot noise level (IQR) is around $I_{noise} = 0.1$ kBit, see Fig. 1c. The modelled signal, I_{sig}, is compared to data in Fig. 2.
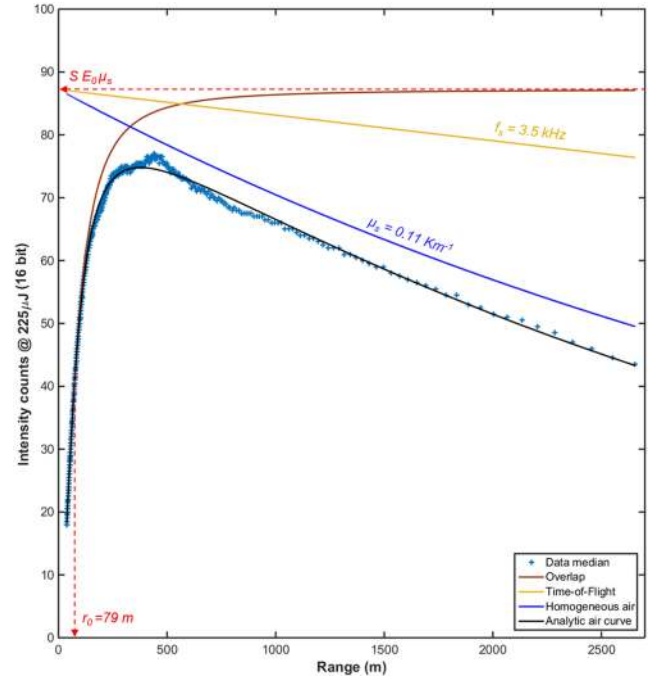

Fig. 2. When the atmosphere is homogenous, the retrieved air signal can be accurately (R^2: 99.98) described by an overlap function, the time-of-flight desynchronization and the atmospheric scatter coefficient. This reduced lidar sensitivity to a single value, S, in units of bits km J^{-1} to be compared to noise bits or across systems.

D. Calibration of Insect Cross Sections and Sizes

Inspired from Radar Cross Sections [48] (RCS), an optical cross section, σ, was introduced [49]. The backscattered cross section quantity is the product of the geometrical cross section from the projected aspect and the diffuse reflectance of a hard target, $\sigma_{back \; scat.} = AR$. Correspondingly the extinction cross section would be the product of area and opacity, $\sigma_{ext.} = A (1\text{-}T) \approx A$ (ballistic light is either scattered or absorbed when transilluminating insects). In our setup $\sigma_{ext.}$ can be seen for vertebrates (Fig. 1a) but is generally below noise threshold for insects. The cross sections are wavelength dependent, and in the near infrared in this study (700-1000 nm) mainly influenced by melanin absorption. In the short wave infrared (1000–1700 nm) it is primary affected by liquid water absorption. When resolved at kHz sampling, the cross sections depend on the phase in the wing beat cycle and can be decomposed into a body envelope and oscillatory part. When wing surface normal coincides with the beam, the spectral cross section can be explained by thin film interference across the spectrum [32], [50]. For more details on lidar light interaction with insects, see [51].

While insect cross sections can be characterized fairly accurately in the laboratory [25], [52], [53], they are challenging to estimate accurately remotely beyond the first digit. Such estimate relies on the assumption that a) the insect is much smaller than the beam, b) that the insect does not transit peripherally and c) that the beam is top-hat rather than Gaussian, see discussion [54]. In practice, the assumptions are partially valid.

At 808 nm the reflectance of most aerofauna is approximately 20% due to melanin [55]. On the other hand, specular conditions

can yield scattering hundreds times relative to a Lambertian white target [32].

Although optical cross section suffers from these deficiencies, it remains as a fairly intuitive measure and one of the few entities to compare between studies, species and instruments. In laboratory, cross sections can be calibrated by white Lambertian Teflon balls [25], [54]. In lidar studies like this, the beam is inaccessible and we calibrate the value against a flat board at a known distance, coated with black diffuse neoprene foam with a reflectance, $R_{term.}$, of 1.8% @ 808 nm.

$$\sigma_{term} = R_{term} \, \sigma_{probe(r_{term})} \qquad (8)$$

Here, σ_{probe}, is the spatial overlapping area of the beam and field of view. We then use the analytical air signal in 7 to extrapolate the lidar sensitivity to other ranges accordingly:

$$\sigma_{insect(r,t)}$$
$$= \frac{\sigma_{term} I_{air(r_{term})} r_{insect}^2 \left(I_{(r_{insect},t)} - I_{air(r_{insect})} \right)}{I_{air(r_{insect})} r_{term}^2 \left(I_{term} - I_{air(r_{term})} \right)} \qquad (9)$$

The equation can be checked by replacing the sub index term *"insect"* with term *"term."*. With the assumption of a homogeneous atmosphere, I_{air} denotes the instrument atmospheric range response. In previous work [20] I_{air} was encountered empirically by the temporal median and could assume any shape, in this work I_{air} is analytical and noise free and derives from system parameters and the momentary atmospheric scattering, $\mu_{s(t)}$. The term σ_{term} denotes a fixpoint with known cross section and range. Such cross section assessment assumes that the insect is fully embedded in the probe volume during the transit. This is generally true, since most insects are small compared to the probe volume of the lidar system, see parameters in Table I. The probe volume is the spatial union of the emitted- and sensed light flux (beam and field-of-view). The r^2 terms in 9 represent the assumption of diffuse Lambertian and omnidirectional scattering from insect and calibration target. We will later return to this discussion.

Apart from cross sections deduced from light intensities, we also successfully applied an additional size measure; apparent size, δ_{insect}. This entity is deduced from opening-angle in the beam and the pixel spread of the echoes according to;

$$p_{cent(t)} = \frac{\sum_{mask} I_{insect(p,t)} p}{\sum_{mask} I_{insect(p,t)}} \qquad (10)$$

$$\delta_{insect(t)} = \frac{r \cos \theta_{sens} l_{pix}}{F_{rec}} \sqrt{\frac{\sum_{mask} I_{insect(p,t)} (p - p_{cent.})^2}{\sum_{mask} I_{insect(p,t)}}}$$

Here, the center pixel, p_{cent}, is calculated by the first statistical moment (center of mass formula, CoM), *mask* denotes the pixels and exposures exceeding the noise level. Apparent size, δ_{insect}, is then calculated as the root of the second statistical moment of the echo (pixel spread) and rescaled by r and the system parameters in Table I. The saturation bound of δ is given by beam width at r, while the lower bound is given by the receiver point spread function (PSF). In principle p_{cent} and δ_{insect} can

assume sub-pixel resolution, in practice both δ and σ are crude size represented approximately only by the first digit.

Since insect envelopes varies from Gaussian- to top hat shapes, and can include specular flashes, we choose to robustly reduce the time dependent size measures $\sigma_{insect(t)}$ and $\delta_{insect(t)}$, by taking the temporal median for their duration of the observation. In addition, note that wingbeats are not resolved in the 300 Hz mode. Hereafter, each observation is represented by a single pair of size measures. Note that apparent size is unaffected by melanin and specular flashes. From their units (see Table I), we understand that $\sigma \propto \delta^2$. A crude estimate of diffuse reflectance of the insects is therefore $R_{insect} \approx \sigma \delta^{-2}$. Although σ is a measure of area, we know that light interacts ballistically with the tissue in the abdomen of small insects such as mosquitoes [53]. This happens when the organism is small in relation to the mean free path in the tissue. This implies that the interaction path-length of the backscattered light is longer and thus more depolarized than for the forward scattered light [53]. In this regime, light scatters from the tissue and eggs [54] inside the insects, and scattering scales additionally with insect thickness. In other words; for small insects, then the retrieved light I_{insect}, originates from the volume and not the area, this would imply a $\sigma \propto \delta^3$ relation.

IV. RESULTS

We mask by a threshold on the instantaneous lidar signal, I_{sig}, when this exceeds the static signal plus three times the noise amplitude (>SNR = 3); $I_{sig(r,t)} > I_{median(r)} + 5 I_{IQR(r)}$. An insect observation is hereafter defined as a connected island in this range-time mask. The procedure is identical to previous work [39], [40]. The range, cross section and apparent size is calibrated as in the previous section.

A. Aerofauna detection in Time and Space

All detected insects are presented in time and space in Fig. 3. As expected, more insects are detected closer to the lidar. However, a pronounced spatial feature, with increased activity, is where the beam passes under the shade of the canopy of the *Ceiba* tree at 516 m distance. This is particularly visible for the 300 Hz measurements. Such monumental trees are known to create a humid micro-climate, shelter and food for both insects and bats [56]. For bats, such trees also provide protection from predators and constitute a landmark and social meeting point in the landscape. We tested observations for detector saturation, and encountered 142 and 21 saturated observations in 300 Hz and 3000 Hz mode respectively. These were predominantly at close range during the rush hour right after sunset but also at longer ranges later in the evening. This period is a popular feeding time for insectivores [28], [29], [56]. In Fig. 3b the counting rates for 300 Hz and 3000 Hz mode is displayed. In the afternoon the curves look surprisingly similar with some 500 observations per minute. The range distribution is however fairly distinct; the 3000 Hz mode generally detects insects at further distances but fails to detect insects in the canopy shade at 516 m. At 19:00 the day of the 300 Hz measurement, the guard at the institute campus switched on the lights at the
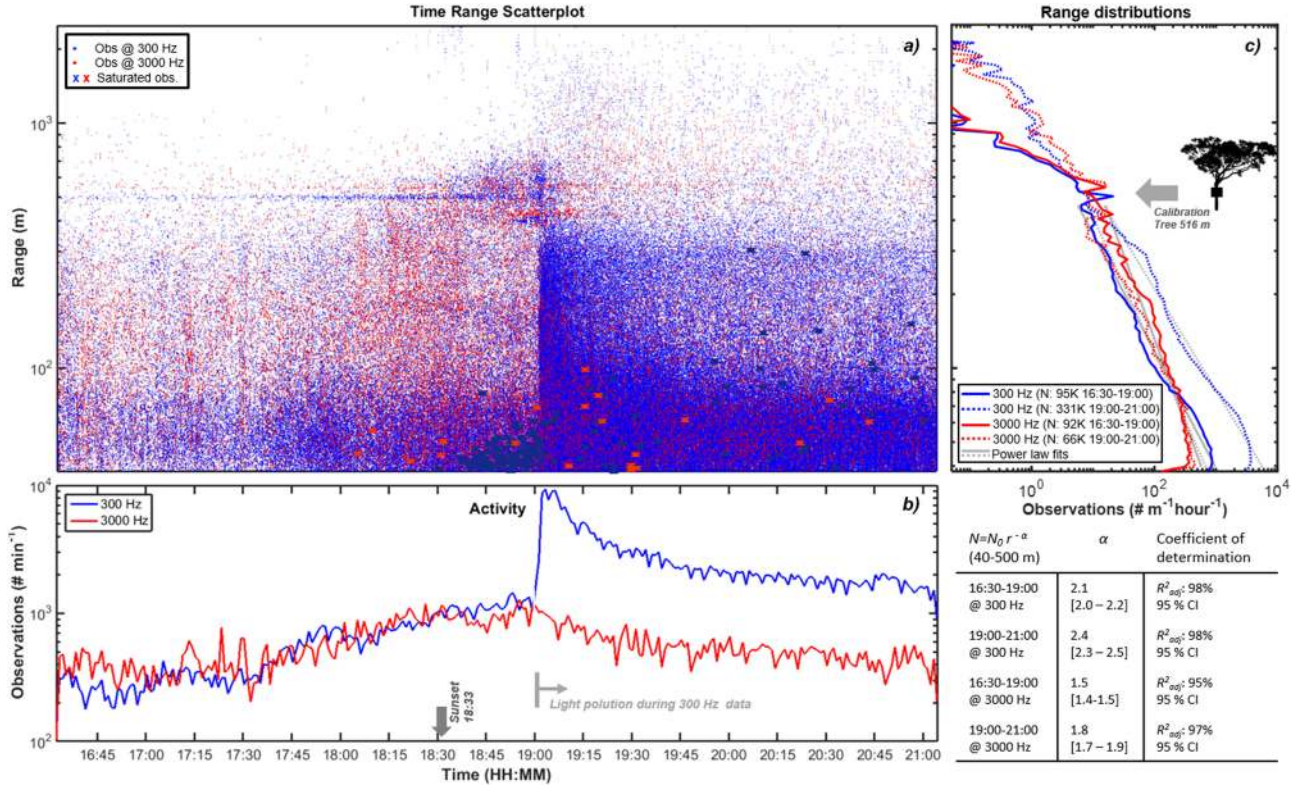
Fig. 3. During 4½ hours, 158244 insects were detected at 3000 Hz rate and 426327 insects were detected at 300 Hz rate. 3a: Display of all observations in time and space. Generally, more insects are detected at close ranges, however, during daytime the shade of the large *Ceiba* tree canopy at 516 m induce increased activity, which is predominantly seen in the long exposure more at 300 Hz. After sunset, this aggregate broadens in the landscape. 3b: Surprisingly, the counting rate is equivalent for 300 Hz and 3000 Hz during the afternoon and after sunset. At 19:00 on the day of the 300 Hz measurements the test range was subject to light pollution. This was not the case for the 3000 Hz measurements. 3c: shows the range distributions of detected insects. Because of the light pollution during the 300 Hz measurements, the data is split in two parts; before and after 19:00.

parking lot (35-90m range). This is a significant light pollution source in the otherwise dark and sparsely populated outskirts of Yamoussoukro. Within a few minutes this drained the remnants of the population under the tree and induced a tenfold increase in activity in the 35-300 m range. Because of this disturbance in the 300 Hz data, we divided both days into two parts before and after the light-pollution event.

The range distributions are displayed in Fig. 3c. The light pollution during the 300 Hz measurements increases the activity in the vicinity (35-300 m), but the range distribution is roughly the same. The activity associated with the tree disappear because of the light pollution, but this is not the case during the day of the 3000 Hz data with no light pollution. At night time, aerofauna is detected at longer distances both for 300 Hz and 3000 Hz measurements and could be due to increased activity of night active bats and moths high over ground (the beam height over ground increases beyond the tree at 516 m). As in previous studies [35], [37], the range distribution can be roughly explained by a power law; $N = N_0 r^{-\alpha}$. We applied this fit for the range between the lidar and the tree with proportions explained (adj-R^2) higher than 96%, see lower right insert in Fig. 3. The aim of this study was to investigate if high pulse energies during long exposures with slow sample rate could be used to detect smaller insects at further distance at the expense of wingbeat information. On the contrary, we now find with significance by

95% confidence intervals (Fig. 3c) that 3000 Hz acquisition gives a lower α value than 300 Hz. Thus 3000 Hz detected more insects far away and the absolute number is identical between the slow and fast rate mode (not considering the light pollution one of the days and not the range tree and beyond). We cannot exclude the possibility that insects behave differently between the days, however. The weather was stable and the probe volume high over ground topography with no obvious landmark preferences apart from the tree. In relation to the range dependence, α, we note that the width- and height of the probe volume, $H_{probe(r)}$ and $W_{probe(r)}$, changes over distance accordingly;

$$W_{probe(r)} = \frac{r \ell_{pix}}{f_{rec}},$$

$$H_{probe(r)} = \delta_{term} \sqrt{1 + \left(\frac{\varnothing_{exp}}{\delta_{term}} - 1 \right) \left(\frac{r - r_{term}}{r_{term}} \right)^2}$$

$$\sigma_{probe} = W_{probe(r)} H_{probe(r)} \approx 40\, r^{0.88}, \quad 40 < r < 500 \tag{11}$$

The width is simply the magnification of the tall pixel footprint, while height is given by the beam waist formula. For the fitted range, the probe volume cross section can be approximated by a power law, the coefficients are in relation to the units in Table I. This expansion will increase the observed abundance
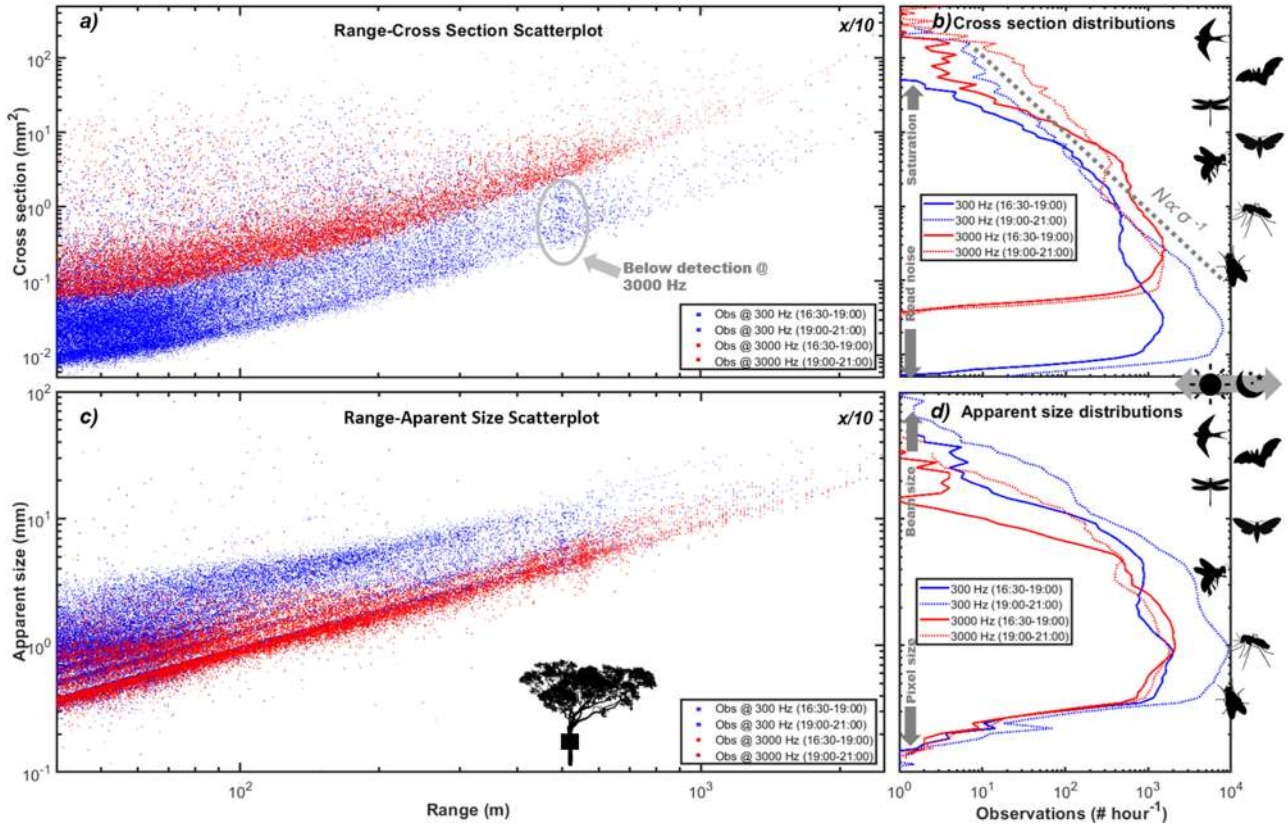
Fig. 4.   Range dependence of detected aero fauna sizes. 4a: Whereas large organisms can be detected in both modes and seldom saturate, smaller insects with smaller cross sections can be seen further away with long exposures at 300 Hz (note the activity under the tree which is not detected in 3000 Hz mode). 4b: The detected biomass is fairly consistent between the overlap in the two modes. In the evening larger organisms are seen at far distance, the distributed is roughly $N \propto \sigma^{-1}$. 4c: The apparent size shares the same minimum in the two modes (note that the red dots are plotted on top), but could be subject to motion blur smearing out features in the distribution in 4d.

for insects up to their maximum detection range. It is, however, not trivial to compensate for the observed numbers because laterally moving insect would increase by H_{probe} and ascending and descending insects would increase by W_{probe}. Still the α values can be compared between the two acquisition modes, since the probe volume is identical.

B. Range Dependence of the Observable Span in the Biomass Size Spectrum

Are the insects seen in the 300 Hz and 3000 Hz data the same? Or could a high dynamic resolution (HDR) approach of stitching together intensities of short and long exposures provide a benefit? Since wingbeat modulation is not resolved in the 300 Hz data, our means of classification are limited to the range and sizing features discussed in Section III.D. In Fig. 4, we plot detection range, r, against the size features σ and δ. Again, we split the data into before and after the light pollution event at 19:00. In order to get a sense of the density of the 584571 observations during the 9 hours, we diluted the scatter plot and only plot every 10th observation in Fig. 4ac. The complete statistics is shown in Fig. 4bd. The cross section, σ, values in Fig. 4ab span three orders of magnitude in each of the modes, limited on the smaller side by detector read-out noise and on the larger side by detector saturation, which is fairly infrequent

($\sim$1‰). This range essentially covers aerofauna from midges, fruit flies, mosquitoes, through bees, moth and dragonflies to bats and swallows (see rough indication in Fig. 4. right pane). At close range the scatterplots in Fig. 4a display flat threshold due to 1. Beyond the range of complete overlap, $r>2r_0$, a clear increasing range dependent threshold of $\sigma_{thrs} \propto r^2$ is seen. This is essentially a consequence of the diffuse assumption in 9. At a couple of km range, the detection limit reaches the larger end of the biomass spectrum.

When lowering the sample rate tenfold, we do indeed see ten times smaller members of the aerofauna. The fact that the remaining and overlapping part of the biomass spectrum is consistent with the fast measurements displaying a reciprocal $N \propto \sigma^{-1}$ behavior [57] gives us confidence in the calibration routines (note that this is not compensated for probe volumes of detectable intervals at different ranges).

In particular, we see that much of the activity in the *Ceiba* tree shade are small insects, that fall below the detection limit at 3000 Hz. This explain the missing feature in Fig. 3a. Admittedly 10^{-2} mm^2 seems small, but low values could arise when exposure times, τ, exceeds transit times, Δt. It could also be dust or pollen, since we could not check for wing beats at 300 Hz.

The range of apparent sizes, δ, is smaller and limited on the small side by the size of the pixel footprints in the atmosphere and by the beam width on the larger side (Fig. 4c). The 300 Hz
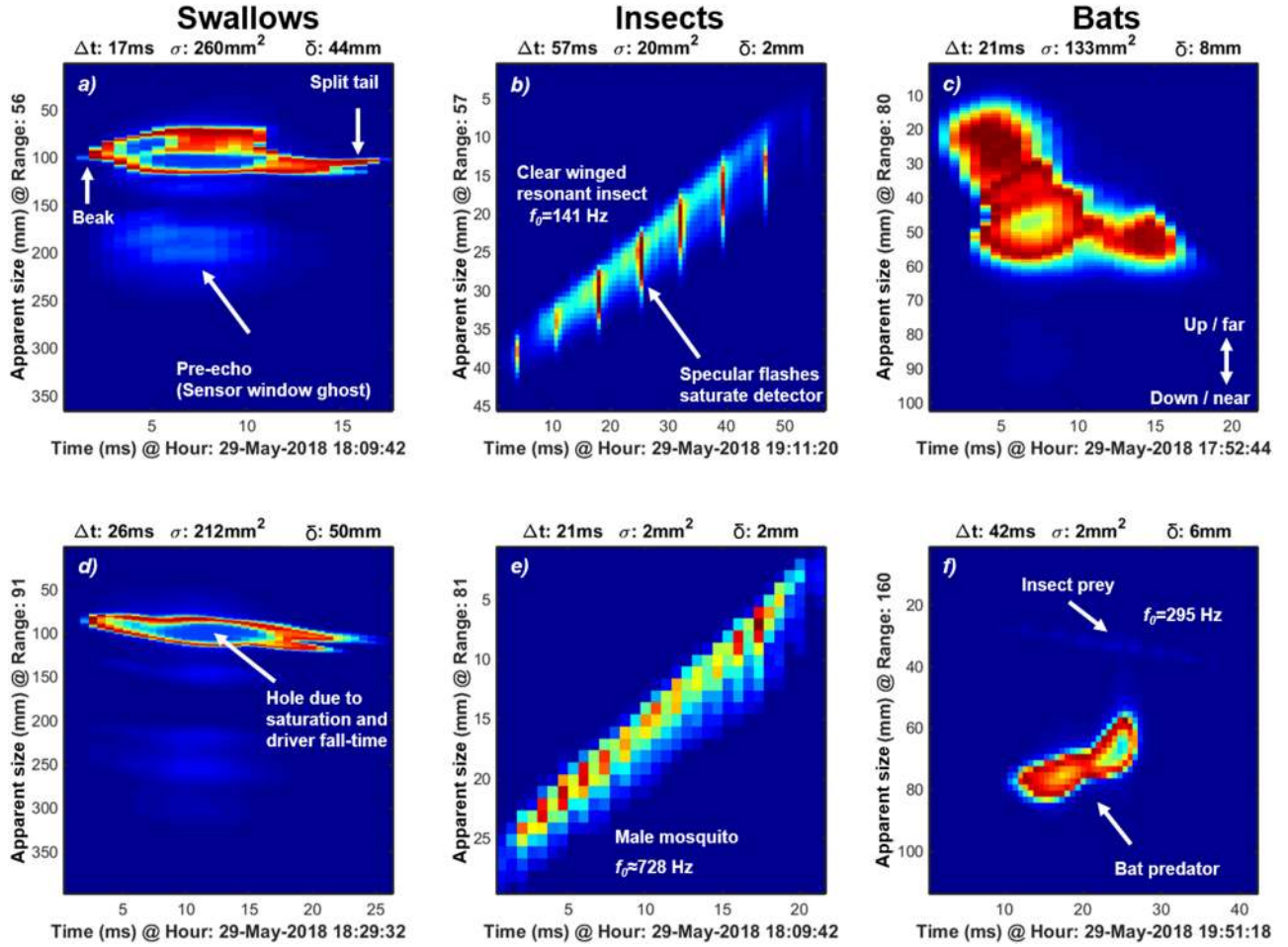
Fig. 5.   The signals of saturated events in the 3000 Hz were inspected individually. Some signals could be associated with swallows, insects and later bats. Not only vertebrates but also specular flashes from insects causes saturation. Note the associated parameters with each event around each subfigure. 5f display both a bat and an insect at 160 m distance.

measurements could be subject to motion blur of the wingbeats (The stripes arise from a pixel rounding operation).

C. Inspection of Saturated Echoes

What caused saturation in entomological lidar? We used the 3000 Hz data and inspected the 21 saturated observations, see selected examples in Fig. 5. In many cases nothing enlightening could be deduced from the signals, but some part of the observation could be attributed to swallows, see Fig. 5ad. When swallows intercept the beam, they are scanned by the lidar line arrays, the observation starting with the beak and ending with the split tail, see Fig. 5ad. Because of the driver leakage between odd and even exposures in combination with the strong signal, it causes substantial signal in the I_{even}, and consequently. the lock-in subtraction produces a hole in the middle of the echo. Not only do strong signals saturate, they also become weaker due to this (this is a hardware issue and can be fixed).

Although birds and bats account for many of the saturated signals, specular flashes from insect wings also saturated the detector in several cases at 3000 Hz, see Fig. 5be. These are peculiar cases, where specular flashes occur in a single 3000

Hz exposure of 310 μs. This occurs when wing surface normal coincides with the beam and when the membrane thickness resonates with the laser in backscattering (this happen when wing thickness is close to either 531, 797, 1063, 1329, 1595 or 1860 nm with a 808 nm lidar). Such flashes would be smeared out in time with the long exposures at 300 Hz rate. The crude reflectance, R_{insect}, of the case in Fig. 5b is 500% compared to Lambertian white. However, the size measures, σ and δ, are temporal medians of the observation, omitting specular flashes. The instantaneous reflectance during the flash (which is hardly resolved in time), is saturated at 1155%. Specular reflectance relate to diffuse reflectance accordingly;

$$R_{Spec.} = \frac{4R_{Lamb.}}{\iint_{-1/2\theta_{rec}}^{1/2\theta_{rec}} \cos(\theta)\, d\theta^2}$$

$$\approx \frac{4R_{Lamb.}}{\theta_{rec}^2} \approx \frac{4R_{Lamb.}r^2}{\varnothing_{rec}^2}, \ \varnothing_{rec} \ll r \qquad (12)$$

Here, the denominator is the fraction of Lambertian reflectance collected by the received light cone, θ_{rec}. The factor 4 is the hemispherical double integral of Lambertian reflectance. At 57 m range a perfect mirror would imply more than a million
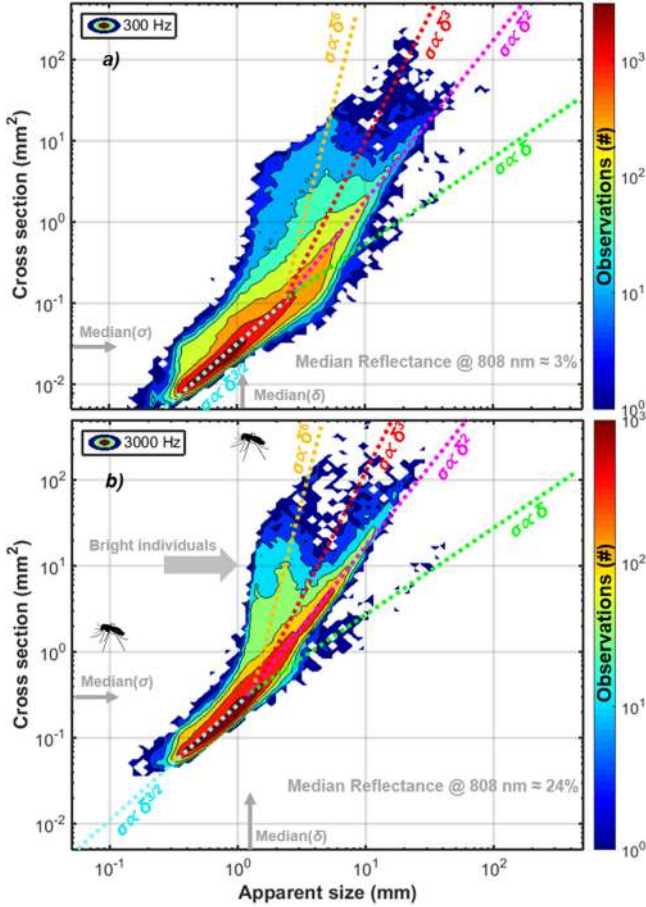
Fig. 6. Covariation of backscatter cross section and apparent size for both 300 Hz and 3000 Hz. Various power relations are displayed ranging from linear relation of saturated observations to quadratic relation from diffuse target to a steep cluster exceeding 100% diffuse reflectance.

percent compared to a diffuse white target. The beam height, parallel to the baseline, can remain collimated up to $r_{farfield\parallel}$ = $0.4\ \lambda^{-1}\emptyset^2_{exp}$ = 5 km (diffraction). The limit for the width is $r_{farfield\vdash} = \emptyset_{exp}F_{exp}\ell^{-1}_{LD}$ = 250m (magnification). From this, we understand that the r^2 attenuation for omnidirectional scattering does not apply to specular flashes from wings which can propagate in a collimated manner. The r^2 attenuation is generally accepted in the lidar community and also appear in 9. But this could explain why we see insects further away and a lower α coefficient for faster rate in Fig. 3. It also leads to a number of issues, e.g., can diffuse cross sections be used? Are oscillatory waveforms in entomological lidar range- dependent?

D. Apparent Sizing and Cross Section

As a final aspect, we looked into the covariance of the two size measures; σ and δ, and we compared the quantities in the slow and fast acquisition mode, see Fig. 6. When considering and comparing the two size measures it is important to think of how they are measured; σ from intensity and δ from pixel spread. Thus a large σ could imply either a large organism or a

shiny organism, whereas large δ could imply a large or a motion blurred observation. The crude median NIR reflectance, $\sigma\delta^{-2}$, for 3000Hz is 24%. This is in accordance with our previous work [25], [55] and can be attributed to melanization. At 300 Hz, median reflectance drops to just 3%, corresponding to the refractive index difference (n_{chitin} = 1.55). Melanin could not absorb 97% at 808 nm, so the losses would need to be explained by transmittance losses in the smaller organisms detected and particularly the fact that the minimum δ is limited by the PSF of a single pixel, so the actual size could be smaller than observed δ. We analyzed the pixel spread (10 without range), in the two cases; 75% of the 3000 Hz observations were focused down to a single pixel, whereas this number was 60% for the 300 Hz observations, due to motion blur from insects. While this verifies the functionality of the Scheimpflug method, it also indicates that δ is not applicable for tiny observations, in particular those picked up in high sensitivity mode. We also investigated whether the wrong median reflectance value in 300 Hz data could arise from transit times shorter than the long exposures, thus diminishing the σ, but we found no indications of increase median reflectance by excluding short observations.

In Fig. 6 we find a main axis of $\sigma \propto \delta^2$ relation which to some extent validates the concept of cross sections [49]. We found that few but large [28] observations pertain to a $\sigma \propto \delta$ axis, and we attribute this both saturation and situation, where the organism size exceeds the probe width, W_{probe}, and thus intensity scales linearly with the pixel spread. We only found limited support for the volumetric scattering $\sigma \propto \delta^3$ from the idea of ballistic interaction [53], also this axis is primarily seen for larger organisms in the 300 Hz mode. It should be considered that e.g., mosquitoes could appear larger in the 300 Hz mode, since the fast wingbeat could increase both σ and δ. In particular, in the 3000 Hz mode we observe a very steep relation of $\sigma \propto \delta^6$. Distinct melanization and observation aspect can change σ a factor three whereas δ would be unaffected. However, it can be seen from Fig. 6 that observations on the $\sigma \propto \delta^6$ ridge exceed 100% diffuse reflectance, thus they must be attributed to specular scattering despite that σ is the temporal median thought to be insensitive to flashes [32]. Finally, we found a $\sigma \propto \delta^{3/2}$ for the tiniest and most numerous observations. We restrain from overinterpreting this, since these are affected by minimum limits and we do not have experience in these small scales.

V. Conclusion and Outlook

We evaluated entomological lidar recordings with slow and fast sample rates, to investigate the dynamic and ranging properties. We could compare the performance although one of the measurement sessions included a light pollution event. We reported more than half a million observations during nine hours at ranges up to couple of kilometers over the Ivorian bush. We provided an accurate analytical explanation for the retrieved air signal during homogeneous conditions. From this, we could reduce the lidar sensitivity to a single value which can be rescaled for laser power and atmospheric conditions and related to noise levels. We have discussed effects and provided

corrections of the time-of-flight roundtrip delay and driver rise time for lock-in detection in Scheimpflug lidar. We revised cross section calibration for diffuse targets.

We could indeed verify that slow rates with long exposures, high laser energies and a just single read-out noise [58], could section smaller organisms in the biomass spectrum and that the overlapping section is in agreement between the two rates. We also demonstrated a case where distant small insects in the tree shade fell under the detection limit of the fast acquisition, but could be detected by the slow sample rate. However, the total number of observations with slow and fast rate was similar, since fast acquisition observed insects significantly further away, we speculate that this is related to rapid flashes of specular scattering dominating over distances. The overlapping region of the biomass spectrum was fairly consistent between slow and fast mode and displayed a plain reciprocal relation $N \propto \sigma^{-1}$.

Through closer inspection of saturated events at 3000 Hz, we could identify large vertebrate insectivores such as swallows and bats. We could also identify insects by wingbeat and demonstrate intensive flashes and realistic size measures for mosquitoes comparing to previous literature [25], [53].

We investigated the covariance of cross section and apparent size. While much of the data supported the idea of a diffuse cross section with a $\sigma \propto \delta^2$ relation, some events did not follow the assumption of smaller organism size than probe volume ($\sigma \propto \delta^2$). Another group displayed diffuse reflectance exceeding 100%, and were interpreted as glossy. This analysis would benefit considerably from a more refined study at fast rate, separating and resolving size contributions from bodies and wings.

From an ecological perspective, we observed the effect of shade of a large tree, which is well-known [56]. After sunset, we could observe how this range feature disperses, and also how a light pollution event drastically changed the insect activity within minutes within ca. 300 m vicinity of the light. In the relatively dark area surrounding the campus, such light pollution would have an impact on the biodiversity [59] and disturb local bat and insect populations [60], [61]. We could identify a predating bat during the dark evening, with a prey with slightly lower wing beat frequencies than mosquitoes. But bats are able to consume around two thousand mosquitoes per night per bat [62]. The presented approach could in principle be used to evaluate bats´ predation on mosquito populations, and hence possible benefits of malaria transmission reduction, but long term seasonal data remains to be seen.

V. Data Availability

The data presented here may be obtained by contacting the authors. The raw data is approximately 500 Gb.

Acknowledgment

References

[1] S. Seibold et al., "Arthropod decline in grasslands and forests is associated with landscape-level drivers," Nature, vol. 574, pp. 671–674, 2019.

[2] C. Rich and T. Longcore, Ecological Consequences of Artificial Night Lighting, United States: Island Press, 2013.

[3] X. Giam, "Global biodiversity loss from tropical deforestation," Proc. Nat. Acad. Sci., vol. 114, pp. 5775–5777, 2017.

[4] V. A. Drake and D. R. Reynolds, Radar Entomology : Observing insect Flight and Migration, Wallingford, Oxfordshire; Boston, MA: CABI, 2012.

[5] W. Daniel Kissling, D. E. Pattemore, and M. Hagen, "Challenges and prospects in the telemetry of insects," Biol. Rev., vol. 89, pp. 511–530, 2014.

[6] G. Hu et al., "Mass seasonal bioflows of high-flying insect migrants," Science, vol. 354, pp. 1584–1587, 2016.

[7] V. A. Drake et al., "Ventral-aspect radar cross sections and polarization patterns of insects at x band and their relation to size and form," Int. J. Remote Sens., vol. 38, pp. 5022–5044, 2017.

[8] I. Potamitis, I. Rigakis, and N.-A. Tatlas, "Automated surveillance of fruit flies," Sensors, vol. 17, pp. 1–14, 2017.

[9] J. Wang et al., "Mosquito counting system based on optical sensing," Appl. Phys. B, vol. 126, p. 10, 2020.

[10] K. Bjerge et al., "A light trap and computer vision system to detect and classify live moths (Lepidoptera) using tracking and deep learning," bioRxiv, 2020.

[11] Y. Zhong et al., "A vision-based counting and recognition system for flying insects in intelligent agriculture," Sensors, vol. 18, pp. 19, 2018.

[12] I. Rigakis, Insectronics, 2020. [Online]. Available: https://www.insectronics.net/

[13] F. Tårnhøj, FaunaPhotonics, 2015. [Online]. Available: www.faunaphotonics.com

[14] M. Brydegaard and S. Svanberg, "Photonic monitoring of atmospheric and aquatic fauna," Laser Photon. Rev., 2018.

[15] K. S. Repasky et al., "Optical detection of honeybees by use of wing-beat modulation of scattered laser light for locating explosives and land mines," Appl. Opt., vol. 45, pp. 1839–1843, 2006.

[16] Z. Guan et al., "Insect monitoring with fluorescence lidar techniques: Field experiments," Appl. Opt., vol. 49, pp. 1–11, 2010.

[17] M. Brydegaard, A. Gebru, and S. Svanberg, "Super resolution laser radar with blinking atmospheric particles – application to interacting flying insects.," Prog. Electromagn. Res., vol. 147, pp. 141–151, 2014.

[18] L. Mei and P. Guan, "Development of an atmospheric polarization scheimpflug lidar system based on a time-division multiplexing scheme," Opt. Lett., vol. 42, pp. 3562–3565, 2017.

[19] M. Brydegaard et al., "The scheimpflug lidar method," SPIE Lidar Remote Sens. for Environ. Monit., vol. 10406, 2017.

[20] M. Brydegaard, A. Gebru, C. Kirkeby et al et al.., "Daily evolution of the insect biomass spectrum in an agricultural landscape accessed with lidar," in Proc. EPJ Web Conferences, 2016, Art. no. 22004.

[21] C. Kirkeby, M. Wellenreuther, and M. Brydegaard, "Observations of movement dynamics of flying insects using high resolution lidar," Sci. Rep., vol. 6, 2016, , Art. no. 29083.

[22] M. Brydegaard et al., "Lidar reveals activity anomaly of malaria vectors during pan-african eclipse," Sci. Adv., 2020.

[23] M. Brydegaard and S. Jansson, "Advances in entomological laser radar," in Proc. IET Intentsional Radar Cenference, 2018.

[24] S. Zhu et al., "Insect abundance over chinese rice fields in relation to environmental parameters, studied with a polarization-sensitive CW near-IR lidar system," ILRC28, 2017.

[25] A. Gebru et al., "Multiband modulation spectroscopy for determination of sex and species of mosquitoes in flight," J. Biophotonics, vol. 11, 2018.

[26] A. P. Genoud et al., "Analysis of predictor variables for mosquito species identification from dual-wavelength polarization-sensitive lidar measurements," in SPIE Asia-Pacific Remote Sens., p. 13, 2018.

[27] C. Kirkeby et al., "Advances in automatic identification of flying insects using optical sensors and machine learning," Sci. Rep., 2020.

[28] E. Malmqvist et al., "The bat-bird-bug battle: Daily flight activity of insects and their predators over a rice field revealed by high resolution scheimpflug lidar," Roy. Soc. Open Sci., vol. 5, 2018.

[29] S. Jansson et al., "A scheimpflug lidar used to observe insect swarming at a wind turbine," Ecological Indicators, vol. 117, 2020, Art. no. 106578.

[30] M. Goerke et al., "Characterizing ice particles using two-dimensional reflections of a lidar beam," Appl. Opt., vol. 56, 2017, pp. G188–G196.

[31] M. Vollmer and J. A. Shaw, "Brilliant colours from a white snow cover," *Phys. Educ.,* vol. 48, pp. 322–331, 2013.

[32] M. Brydegaard *et al.*, "Can the narrow red bands of dragonflies be used to perceive wing interference patterns?," *Ecol. Evol.,* vol. 8, pp. 5369–5384, 2018.

[33] J. A. Shaw *et al.*, "Polarization lidar measurements of honey bees in flight for locating land mines," *Opt. Exp.,* vol. 13, pp. 5853–5863, 2005.

[34] Z. Liu *et al.*, "Preliminary studies on atmospheric monitoring by employing a portable unmanned Mie-scattering scheimpflug lidar system," *Remote Sens.,* vol. 11, pp. 837, 2019.

[35] K. Rydhmer *et al.*, "Lidar profiling of bee activity patterns and foraging distributions," *Animal Telemetry*, Submitted 2020.

[36] M. J. Tauc *et al.*, "Field demonstration of a wing-beat modulation lidar for the 3D mapping of flying insects," *OSA Continuum,* vol. 2, 2019, pp. 332–348.

[37] S. Jansson *et al.*, "Real-time dispersal of malaria vectors in rural africa monitored with lidar," *PLoS One,* 2020.

[38] B. K. Kouakou *et al.*, "Entomological scheimpflug lidar for estimating unique insect classes in-situ field test from ivory coast," *OSA Continuum,* vol. 3, pp. 2362–2371, 2020.

[39] E. Malmqvist, "From fauna to flames: Remote sensing with scheimpflug lidar," Lund, Sweden: Lund Univ., 2019.

[40] S. Jansson, "Entomological lidar: Target characterization and field applications," Lund, Sweden: Lund Univ., 2020.

[41] Y. Li *et al.*, "Insect flight velocity measurement with a CW near-IR scheimpflug lidar system," *Opt. Exp.,* vol. 28, pp. 21891–21902, 2020.

[42] G. Zhao *et al.*, "Dual-band continuous-wave lidar system employed for particle classification," *Appl. Opt.,* vol. To appear, 2018.

[43] L. Mei and M. Brydegaard, "Atmospheric aerosol monitoring by an elastic scheimpflug lidar system," *Opt. Exp.,* vol. 23, pp. A1613–A1628, 2015.

[44] E. Malmqvist *et al.*, "Scheimpflug lidar for combustion diagnostics," *Opt. Exp.,* 2018.

[45] J. Larsson *et al.*, "Atmospheric CO2 sensing using Scheimpflug-lidar based on a 1.57um fiber source," *Opt. Exp.,* vol. 27, pp. 17348–17358, 2019.

[46] K. Stelmaszczyk *et al.*, "Analytical function for lidar geometrical compression form-factor calculations," *Appl. Opt.,* vol. 44, pp. 1323–1331, 2005.

[47] S. Zhu *et al.*, "Insect abundance over chinese rice fields in relation to environmental parameters, studied with a polarization-sensitive CW near-IR lidar system," *Appl. Phys. B,* vol. 123, 2017.

[48] J. Riley, "Angular and temporal variations in the radar cross-sections of insects," in *Proc. Inst. Elect. Engineers*, 1973, pp. 1229–1232.

[49] M. Brydegaard, "Towards quantitative optical cross sections in entomological laser radar – potential of temporal and spherical parameterizations for identifying atmospheric fauna," *PLoS One,* vol. 10, 2015, Art. no. e0135231.

[50] D. G. Stavenga, "Thin film and multilayer optics cause structural colors of many insects and birds," *Mater. Today: Proc.,* vol. 1, pp. 109–121, 2014.

[51] M. Brydegaard and S. Svanberg, "Photonic monitoring of atmospheric and aquatic fauna," *Laser Photon. Rev.,* 2018, Art. no. 1800135.

[52] M. Li *et al.*, "Bark beetles as lidar targets and prospects of photonic surveillance," *J. Biophotonics,* 2020.

[53] S. Jansson *et al.*, "First polarimetric investigation of malaria mosquitos as lidar targets," *IEEE JSTQE Biophotonics,* vol. 25, pp. 1–8, 2018.

[54] A. P. Genoud *et al.*, "Identification of gravid mosquitoes from changes in spectral and polarimetric backscatter cross-sections," *J. Biophotonics*, 2019, Art. no. e201900123.

[55] M. Brydegaard, "Advantages of shortwave infrared LIDAR entomology," in *Proc. Imag. Appl. Opt.*, 2014, Art. no. LW2D.6.

[56] J. Rydell, A. Entwistle, and P. A. Racey, "Timing of foraging flights of three species of bats in relation to insect activity and predation risk," *Oikos,* pp. 243–252, 1996.

[57] W. P. Hooper and G. M. Frick, "Lidar detected spike returns," *J. Appl. Remote Sens.,* vol. 4, no. 1, 2010, Art. no. 043549.

[58] L. Mei, Z. Kong, and P. Guan, "Implementation of a violet scheimpflug lidar system for atmospheric aerosol studies," *Opt. Exp.,* vol. 26, pp. A260–A274, 2018/Mar./19 2018.

[59] F. Hölker *et al.*, "Light pollution as a biodiversity threat," *Trends Ecol. Evol.,* vol. 25, pp. 681–682, 2010.

[60] J. Rydell, J. Eklöf, and S. Sánchez-Navarro, "Age of enlightenment: Long-term effects of outdoor aesthetic lights on bats in churches," *Roy. Soc. open Sci.,* vol. 4, 2017, Art. no. 161077.

[61] J. Rydell *et al.*, "Bats roosting – Switch-off the lights, please!," *Afr. Conservation Telegraph,* vol. 15, 2019.

[62] J. Rydell, D. P. McNeill, and J. Eklöf, "Capture success of little brown bats (Myotis lucifugus) feeding on mosquitoes," *J. Zool.,* vol. 256, pp. 379–381, 2002.

Mikkel Brydegaard was born in Copenhagen, Denmark, in 1980. He received the M.Sc. degree in electrical engineering, the Ph.D. degree in atomic physics and the Docent degree from Lund University, Lund, Sweden in 2007, 2012, and 2015, respectively. He has experience in instrumentation, optical spectroscopy, bio-photonics, remote sensing, and applied mathematics. During postgraduate years, he was with Stellenbosch University, Stellenbosch, South Africa, and University of Oslo, Oslo, Norway, for his research, and his work was focused on lidar monitoring of aero-fauna, in particular contributing with the Scheimpflug lidar method. He is currently a Principal Investigator with the Department of Physics and Department of Biology, and a Senior Researcher with Norsk Elektro Optikk. He was the Co-Founder of FaunaPhotonics, Denmark, and African Spectral Imaging Network.

Benoit Kouakou was born in Adjamé, Abidjan, Côte d'Ivoire in 1980. He received the bachelor's degree in applied and fundamental science in 2009 and the master's degree in photonics from the University of Nangui Abrogoua, Abidjan, Côte d'Ivoire, in 2015. He is currently working toward the Doctoral degree in entomological remote sensing and spectroscopy with National Polytechnic Institute, Yamoussoukro, Côte d'Ivoire.

Samuel Jansson was born in Stockholm, Sweden, in 1988. He received the M.Sc. degree in engineering physics and the Ph.D. degree in optical remote sensing of insects from the Department. of Physics, Lund University, Lund, Sweden, in 2015 and 2020 respectively. He has authored or coauthored 22 papers, obtained one patent, and co-supervised four student thesis. He is currently a Researcher with the Department of Biology, Lund University. His research interests include entomological lidar, radar, and machine learning techniques, and their applications in studying vector ecology, migration ecology, and insect decline.

Jens Rydell was born in Sweden in 1953. He received the Ph.D. degree in animal ecology from Lund University, Lund, Sweden, in 1990. In 1998, he was an Associate. Professor of zoology with Gothenburg University, Gothenburg, Sweden. His research interests include the biology of bats and insects with the focus on ultrasonic echolocation and communication, specifically bat–insect interactions, which was granted by the Swedish Research Council 1992–2005. Since 2009, his research has been granted by the Swedish Energy Agency, with a focus on the environmental consequences of wind farming and designing mitigation measures to minimize the killing of bats. He was also engaged in the research on the negative effect of light pollution on nocturnal animals, specifically bats. He has authored or coauthored 150 refereed research papers, several books, and other articles. He was the recipient of the Swedish Research Council Researcher Award in 2000, the Royal Swedish Academy of Science Conservation Award in 2017, and the Skåne Wind Farming Academy Prize in 2017.

Jeremie Zoueu received the M.S. degree in laser engineering with Galilee Institute, University of Paris XIII, Villetaneuse, France, in 1992 and the Ph.D. degree in physics, in the field of lasers and photonic materials, from Pierre & Marie Curie University, Paris, France, in 1996. He is currently a Professor of photonics with the National Polytechnic Institute(INP-HB), Yamoussoukro, Cote d'Ivoire. He is currently the Director with the Interdisciplinary Research and Innovation Unit and the Founder and Head with the Instrumentation, Imaging, and Spectroscopy Laboratory, INP-HB. On the international level, he is the Coordinator of the African Spectral Imaging Network and also an Affiliate Faculty with Virginia Commonwealth University, Richmond, VA, USA. He is the Co-Founder of African Spectral Imaging Network.